DISCRETE MODELS OF FLUIDS: SPATIAL AVERAGING, CLOSURE AND MODEL REDUCTION

ALEXANDER PANCHENKO* AND ALEXANDRE TARTAKOVSKY †

Abstract. The main question addressed in the paper is how to obtain closed form continuum equations governing spatially averaged dynamics of semi-discrete ODE models of fluid flow. In the presence of multiple small scale heterogeneities, the size of these ODE systems can be very large. Spatial averaging is then a useful tool for reducing computational complexity of the problem. The averages satisfy balance equations of mass, momentum and energy. These equations are exact, but they do not form a continuum model in the true sense of the word because calculation of stress and heat flux requires solving the underlying ODE system. To produce continuum equations that can be simulated without resolving micro-scale dynamics, we developed a closure method based on the use of regularized deconvolutions. We mostly deal with non-linear averaging suitable for Lagrangian particle solvers, but consider Eulerian linear averaging where appropriate. The results of numerical experiments show good agreement between our closed form flux approximations and their exact counterparts.

Key words. multiphase flow simulation, multiscale computational methods, upscaling, model reduction, dimension reduction, volume averaging, closure

AMS subject classifications. 82D25, 34K33, 35B27, 35L75, 35Q30, 35Q70, 37Mxx, 37N10, 70F10, 70Hxx, 74Q10, 82C21, 82C22

1. Introduction.

Direct simulation of heterogeneous fluid flows can be very costly because of the need to resolve numerous small scale features. In applications, this situation often occurs when dealing with viscous turbulence and flows of multiphase mixtures. Increasing demand for large-scale simulations of such media spurs the development of complexity reduction methods and multiscale algorithms. The literature on multiscale methods is large and diverse, and we do not attempt a complete survey. The approaches that are most relevant to this study are derivation of hydrodynamics equations from molecular models [12], large eddy simulation for Navier Stokes equations [2], and volume averaging for mixtures [4], [5], [14], [39].

The development of the first theme was motivated by an important problem of physics: establishing a link between phenomenological constitutive equations and underlying molecular dynamics. An elegant approach to this problem was proposed by Irving and Kirkwood [12], Noll [29], and developed further by Hardy [10] and Murdoch and Bedeaux [25], [26], [27], [28]. They observed that space-time averages such as density, momentum, and energy satisfy continuum mechanical balance equations. These equations are exact, and stress and heat flux are given explicitly in terms of particle positions and velocities. Such equations can be very useful for linking microscale dynamics with mesoscale phenomena, but they do not provide a satisfactory continuum model. Indeed, to evaluate the fluxes, one must have complete knowledge of the underlying particle dynamics. Thus the main advantage of the continuum description, complexity reduction, is not achieved. In classical continuum mechanics, there is no need to find trajectories of all atoms because phenomenological constitutive equations express fluxes in terms of density, velocity, deformation, and temperature. Accordingly, the *closure problem* is posed as follows: find accurate approximations of the exact fluxes by constitutive equations.

In the paper, we address this problem for ODE models of fluid flow. We study two basic groups of models. The first is dissipative Newton equations generated by meshless Lagrangian particle solvers, such as Smoothed Particle Hydrodynamics (SPH) [35], [37]. The ODEs in SPH are similar to the equations of molecular dynamics.

The second group contains ODE systems obtained by Eulerian finite difference or finite element discretizations. Eulerian averaging is similar to the large eddy simulation (LES) of viscous turbulent flows. Just as in the molecular dynamics averaging, the main difficulty is finding a good closure model for the extra convective stress induced by the velocity fluctuations. Recently proposed deconvolution closure [1], [2] is particularly close to the method developed in this paper.

Volume averaging was developed in the continuum mechanics community. Its application to complex fluids and mixtures is similarly hindered by the lack of a general theory for deriving closure models. This

*Department of Mathematics, Washington State University, Pullman, WA 99164 (panchenko@math.wsu.edu).

†Computational Mathematics Group, Pacific Northwest National Laboratory, Richland, WA 99352 (alexandre.tartakovsky@pnl.gov).

is particularly important for mixture theory [4], [14] where averaging produces interaction fluxes describing mass, momentum and energy exchange between the phases. These terms are much more difficult to measure experimentally than, say, shear viscosity. Empirical closures for interaction terms contain undetermined constants that must be calibrated using limited experimental data and a few simulated examples. As a result, ad hoc models used in the literature do not work in many situations of practical interest [39].

Overall, our approach was shaped by three considerations. First, we tried to minimize the role of ad hoc assumptions in the closure equations. As a result, our theory has no undetermined constant parameters. Second, we wanted to find a way to balance cost and accuracy. At present, we do not have complete error estimates, but the examples presented below show how better accuracy can be achieved by increasing the operation count. Third, acknowledging the shift from phenomenological modeling to computational thinking, we favor computational utility over other factors. The main criteria for choosing models are operation count and incurred error. Consequently, we did not use truncated Taylor expansions in the constitutive equations. From the purely computational point of view, linearized constitutive equations may increase the error (in comparison with the exact balance equations of particle averaging), while the associated savings are negligible. Somewhat surprisingly, this pragmatic approach yields interesting non-local and nonlinear continuum models [30], [31] that are similar to peridynamics [19], [32], [33].

The closure method studied in the paper uses regularization methods for solving convolution integral equations of the first kind. The kinematic averages (density and linear momentum) are related to the interpolants of microscale variables via a linear convolution operator. The kernel of this operator is the "window function" used to generate averages. Such integral operators are usually injective and compact. Injectivity implies existence of a single-valued inverse operator, but this inverse operator is not continuous. In practice this means that small perturbation of the right hand side my lead to large perturbations in the computed solution. Therefore, the deconvolution problem is ill-posed. Such problems and regularization solution methods are well studied [3, 9, 11, 16, 23, 38]. A particular regularization used in this paper is Landweber iteration [7], [17].

The use of regularization for closure in molecular dynamics applications was proposed in [31], where we also conducted numerical tests of the simplest zero-order closure (similar to the Cauchy-Born rule (see, e. g. [20]), and the quasi-continuum method [21], [34]). Another paper [36] contains an application of the zero-, first- and second-order approximations to dissipative, second order ODE systems representing meshless discretizations of fluid flows. In this article we continue the investigation of fluid models started in [36]. We study both first- and second order ODE systems, representing, respectively, spatial (Eulerian) and referential (Lagrangian) discretizations. Both low order and higher order closures are considered.

Our method has some similarities with seamless multiscale methods [6] and equation-free methods [15]. The difference between our method and these approaches is in the use of fine scale computing. Both seamless and equation-free methods require solving the underlying fine scale system. This is done either intermittently (equation-free method) or using a small number of time steps (seamless method). Within our approach, the fine scale equations are not solved at all.

In Sections 7 and 8 we present three examples. The first example is a model of viscous flow in a pipe. This example is simple, so the average velocity and stress can be calculated explicitly. This allows us to study convergence of regularizations and see how different Fourier modes are transformed by averaging and deconvolution. We show that the error depends on the frequency content of the initial conditions, and more iterations are needed to adequately deconvolute more oscillatory velocities.

Next, we consider a channel flow of a fluid with a periodic rapidly oscillating viscosity. Since homogenization approximation [13] is available, most quantities of interest can be calculated explicitly. Compared to the previous example, the new feature here is the presence of high frequency oscillations in the velocity, even for low-frequency initial conditions. High frequency modes of the velocity contribute significantly to the low frequency modes of the viscous stress. So, to reproduce the average stress, we must reconstruct high frequency content of the micro-scale velocity from the given average velocity. Strong attenuation of high frequencies during averaging increases the risk of runaway instability. To improve the situation, we propose to use filtering. It selectively boosts a range of high frequencies that are important for capturing low frequency content of the stress. Since the period of viscosity oscillations is known, we can determine beforehand the frequency band that has to be filtered. The knowledge of the relevant frequencies also helps to design the filter so that we have just enough, but not too much boost.

An important application of closure is development of fast numerical methods for simulating mesoscopic continuum dynamics of large ODE systems. Mesoscale solvers employ coarser meshes and larger time steps than direct ODE solvers. This leads to a more efficient simulation of the relevant average quantities. Our third example is a complete meso-scale simulation of a layered flow of a two-fluid mixture. The number of layers is large, but unlike the second example, here we consider layers of different widths varying from very small to rather large. The constitutive equations for both phases employ Newton's law for the viscous stress, and van der Waals equation of state for the pressure, so the overall constitutive behavior of each fluid is non-Newtonian. We use a low-order deconvolution with no filtering, but the meso-solver still produces a good agreement with the directly simulated average velocity. The computational savings are estimated here as well. The operation count of the meso-solver per time step scales as $O(1)$ as the number of fluid particles N approaches infinity. This compares favorably with the linear scaling for the direct simulation. Additional savings are produced by using time steps that are approximately 32 times larger than in the direct simulation.

The paper is organized as follows. In Section 2 we define the relevant length scales and non-dimensional resolution parameters. Section 3 contains the description of the fine scale ODE models. Averaging methods are described in Section 4. Section 5 is devoted to the derivation of integral approximations for various averages. In Section 6, we describe regularized deconvolution closure methods. Section 7 contains examples of closure. An example of a meso-scale simulation is presented in Section 8. Finally, conclusions are provided in Section 9.

2. Length scales. Our goal is to approximate dynamics of various mesocopic spatial averages (density, velocity, stress etc). In this paper we focus on spatial averages. The averages are functions of the particle (node) positions $\boldsymbol{q}_j(t)$ and velocities $\boldsymbol{v}_j(t)$. Suppose that $\boldsymbol{q}_j$ remain inside a bounded domain Ω during the observation time T and denote Euclidean coordinates in Ω by $\boldsymbol{x}$.

Since averages are scale-dependent, we define three length scales:
- macroscopic length scale L is a typical size (diameter) of Ω;
- mesoscopic length scale ηL where η is a parameter characterizing mesoscale spatial resolution;
- microscopic length scale εL with

$$\varepsilon = N^{-1/d}. \tag{2.1}$$

Here N is the number of particles, and d is the dimension of the physical space, usually 1, 2, or 3. For numerical experiments we will mostly use $d = 2$.

To ensure scale separation, we require

$$\varepsilon \ll \eta \ll 1 \tag{2.2}$$

When time averaging is desired, one can similarly define a mesoscopic time scale λT where T is the observation time and $\lambda \ll 1$ characterizes mesoscopic temporal resolution.

3. ODE models of fluid flow. We consider two types of ODE models that can be loosely termed Eulerian and Lagrangian.

3.1. Eulerian semi-discretization. These are ODE systems of the form

$$\dot{\boldsymbol{v}}_i = \boldsymbol{F}_i(t, \boldsymbol{V}), \tag{3.1}$$

where $\boldsymbol{v}_i$ are node velocities, $\boldsymbol{V}$ is a vector containing all $\boldsymbol{v}_i$, and $\boldsymbol{F}_i$ are formed by discretizing spatial derivatives if the PDE model of the flow. For example, for Navier Stokes equations,

$$\boldsymbol{F}_i = -\boldsymbol{v}_i \cdot (\nabla_h \boldsymbol{v})_i - \frac{\nabla_h P_i}{\rho_i} - \frac{1}{\rho_i} \mathrm{div}_h \left(2\mu e_h(\boldsymbol{v})_i + \boldsymbol{f}_i^{(ext)} \right) \tag{3.2}$$

where operators with the subscript h denote finite difference discretizations of the corresponding differential operators. Also, P_i are node values of pressure, ρ_i are node values of density, and $e(\boldsymbol{v}) = \frac{1}{2}(\nabla \boldsymbol{v} + \nabla^T \boldsymbol{v})$. Also, $\boldsymbol{f}_i^{(ext)}$ denote external forces, such as gravity.

3.2. Lagrangian semi-discretizations. In a particle solver, such as smooth particle hydrodynamics (SPH) [22], a fluid is approximated by a collection of interacting fluid particles. The particles with constant masses m_i are characterized by positions $\boldsymbol{q}_i$ and velocities $\boldsymbol{v}_i$. The equations of motion are Newton equations

$$\dot{\boldsymbol{q}}_i = \boldsymbol{v}_i, \tag{3.3}$$

$$m_i \dot{\boldsymbol{v}}_i = \boldsymbol{f}_i + \boldsymbol{f}_i^{(ext)}, \tag{3.4}$$

The interparticle forces $\boldsymbol{f}_i$ are sums of the pair forces $\boldsymbol{f}_{ij}$ that depend on the relative positions and velocities. For example, Navier Stokes equations can be well approximated ([37]) by using forces

$$\boldsymbol{f}_{ij} = -\left(\frac{P_i}{n_i^2} + \frac{P_j}{n_j^2}\right) \nabla_i w(\boldsymbol{q}_i - \boldsymbol{q}_j) + 2\mu \frac{\boldsymbol{v}_i - \boldsymbol{v}_j}{n_i n_j |\boldsymbol{q}_i - \boldsymbol{q}_j|^2} (\boldsymbol{q}_i - \boldsymbol{q}_j) \cdot \nabla_i w(\boldsymbol{q}_i - \boldsymbol{q}_j). \tag{3.5}$$

Here w is the window function that is used in micro-scale averaging, P_i and $n_i = \sum_{j \neq i} w(\boldsymbol{q}_i - \boldsymbol{q}_j)$ are, respectively, pressures and number densities associated with a particle i. The pressure must be given by an equation of state $P_i = P(n_i)$.

4. From discrete models to hydrodynamical averages.

4.1. Non-linear averaging. Non-linear averaging was pioneered by Noll and Hardy [10] and later developed by Murdoch and Bedeaux [25], [28]. In this subsection we recall the basics of the method and introduce the relevant notation. Fix a smooth function $\psi(\boldsymbol{x})$ that will be used to generate averages. It is normalized so that

$$\int \psi(\boldsymbol{x}) d\boldsymbol{x} = 1,$$

and decays sufficiently fast as $|\boldsymbol{x}| \to \infty$. Next, set $\psi_\eta(\boldsymbol{x}) = \eta^{-d} \psi\left(\frac{\boldsymbol{x}}{\eta}\right)$. Many choices of ψ are possible, but in this paper we prefer to work with Gaussian ψ, so that

$$\psi_\eta(\boldsymbol{x}) = \frac{1}{(\sqrt{\pi}\eta)^d} e^{-\frac{\boldsymbol{x}\cdot\boldsymbol{x}}{\eta^2}}. \tag{4.1}$$

The average density and linear momentum are defined by, respectively,

$$\overline{\rho}^\eta(t, \boldsymbol{x}) = \sum_{j=1}^N m_j \psi_\eta(\boldsymbol{x} - \boldsymbol{q}_j(t)), \tag{4.2}$$

$$\overline{\rho}^\eta \overline{\boldsymbol{v}}^\eta(t, \boldsymbol{x}) = \sum_{j=1}^N m_j \boldsymbol{v}_j(t) \psi_\eta(\boldsymbol{x} - \boldsymbol{q}_j(t)). \tag{4.3}$$

Differentiating $\overline{\rho}^\eta$ and $\overline{\rho}^\eta \overline{\boldsymbol{v}}^\eta$ in time and using the ODEs (3.3), (3.4) one can obtain mesoscopic balance equations (MPDEs):

$$\partial_t \overline{\rho}^\eta + \mathrm{div}(\overline{\rho}^\eta \overline{\boldsymbol{v}}^\eta) = 0, \tag{4.4}$$

and the momentum balance equation

$$\partial_t(\overline{\rho}^\eta \overline{\boldsymbol{v}}^\eta) + \mathrm{div}(\overline{\rho}^\eta \overline{\boldsymbol{v}}^\eta \otimes \overline{\boldsymbol{v}}^\eta) = \mathrm{div}\boldsymbol{T}^\eta + \boldsymbol{F}^{(ext)}. \tag{4.5}$$

The stress $\boldsymbol{T}^\eta$ is given by ([28]):

$$\boldsymbol{T}^\eta = \boldsymbol{T}^\eta_{(c)} - \boldsymbol{T}^\eta_{(int)},$$

where $\boldsymbol{T}^{\eta}_{(c)}$ is the convective stress

$$\boldsymbol{T}^{\eta}_{(c)}(t,\boldsymbol{x}) = \sum_{j=1}^{N} m_j(\overline{\boldsymbol{v}}^{\eta} - \boldsymbol{v}_j) \otimes (\overline{\boldsymbol{v}}^{\eta} - \boldsymbol{v}_j)\psi_{\eta}(\boldsymbol{x} - \boldsymbol{q}_j) \tag{4.6}$$

and $\boldsymbol{T}^{\eta}_{(int)}$ is the interaction stress

$$\boldsymbol{T}^{\eta}_{(int)}(t,\boldsymbol{x}) = \sum_{(j,k)} \boldsymbol{f}_{jk} \otimes (\boldsymbol{q}_k - \boldsymbol{q}_j) \int_0^1 \psi_{\eta}\left(s(\boldsymbol{x} - \boldsymbol{q}_k) + (1-s)(\boldsymbol{x} - \boldsymbol{q}_j)\right) ds. \tag{4.7}$$

The summation in j,k is over all pairs of particles (j,k) that interact with each other. The external force is given by

$$\boldsymbol{F}^{(ext)}(t,\boldsymbol{x}) = \sum_{i=1}^{N} \boldsymbol{f}_i^{(ext)} \psi_{\eta}(\boldsymbol{x} - \boldsymbol{q}_i). \tag{4.8}$$

Discretizing spatial derivatives in (4.4)-(4.8) on the mesoscopic mesh yields a system of ODEs, called the *meso-system*, written for mesh values of $\overline{\rho}^{\eta}_j$, $(\overline{\rho}^{\eta}\overline{\boldsymbol{v}}^{\eta})_j$ and $\boldsymbol{T}^{\eta}_j$. The dimension of the meso-system is much smaller than the dimension of the original ODE problem, since the mesoscale mesh size is much larger than a typical interparticle distance. But this fact alone does not reduce the complexity, because one must know positions and velocities of all particles to evaluate stress in (4.6), (4.7). To eliminate the need for simulating particle trajectories, one can approximate the exact stress by an operator acting on the average density and velocity. The procedure of generating such approximations can be termed a closure method.

4.2. Linear averaging. Linear average of the velocity is defined as

$$\overline{\overline{v}}(t,\boldsymbol{x}) = \frac{|\Omega|}{N} \sum_{i=1}^{N} \psi_{\eta}(\boldsymbol{x} - \boldsymbol{y}_i)\boldsymbol{v}_i(t), \tag{4.9}$$

where $\boldsymbol{y}_i$ are mesh nodes. For sufficiently fine meshes, the sum can be approximated by an integral

$$\overline{\overline{v}}(t,\boldsymbol{x}) \approx \int \psi_{\eta}(\boldsymbol{x} - \boldsymbol{y})\boldsymbol{v}(t,\boldsymbol{y})d\boldsymbol{y}. \tag{4.10}$$

This integral averaging is extensively used in large eddy simulation (LES) of turbulent flows (see e.g. [2]). The governing equations for the averages are derived in a straightforward manner. Structurally, they resemble the PDEs underlying (3.1). Similarly to (4.4)-(4.8), these equations are not in closed form, and finding a good closure for averaged Navier Stokes equations is the subject of active research in LES.

5. Integral Approximations of averages. To exploit the special structure of non-linear averages, it is convenient to approximate sums such as

$$\overline{g}^{\eta} = \frac{1}{N} \sum_{j=1}^{N} g(\boldsymbol{v}_j, \boldsymbol{q}_j)\psi_{\eta}(\boldsymbol{x} - \boldsymbol{q}_j) = \frac{1}{|\Omega|} \frac{|\Omega|}{N} \sum_{j=1}^{N} g(\boldsymbol{v}_j, \boldsymbol{q}_j)\psi_{\eta}(\boldsymbol{x} - \boldsymbol{q}_j) \tag{5.1}$$

by integrals. The sum in (5.1) resembles a Riemann sum for $|\Omega|^{-1} g\psi_{\eta}(\boldsymbol{x} - \cdot)$. However, because of the motion of particles, (5.1) is not in general a Riemann sum. A proper Riemann sum should be generated by a partition of Ω into cells of equal volume where each cell contains exactly one particle. In one dimension, the domain is an interval, say $(0, L)$ and the cells are intervals of length L/N. Thus, if the distance between two particles is less than L/N, then the desired partition does not exist. For two- and three-dimensional domains, it may be possible to use more general partitions, but for particles that are spaced non-uniformly, the shapes of these cells may be quite far from slightly deformed rectangles, which would make it difficult to estimate the accuracy of the resulting integral approximation.

A better approach is to make use of a microscopic flow map and the associated Jacobian describing local volume changes. Let $\tilde{\boldsymbol{q}}(t,\boldsymbol{X}),\tilde{\boldsymbol{v}}(t,\tilde{\boldsymbol{q}})$ be suitable position and velocity interpolants, associated with the system (3.3), (3.4). At $t=0$ these interpolants satisfy

$$\tilde{\boldsymbol{q}}(0,\boldsymbol{X}_j)=\boldsymbol{q}_j^0, \qquad \tilde{\boldsymbol{v}}(0,\tilde{\boldsymbol{q}}(0,\boldsymbol{X}_j))=\boldsymbol{v}_j^0,$$

where $\boldsymbol{X}_j$, $j=1,2,\ldots,N$ are points of ε-periodic rectangular lattice in Ω. At other times,

$$\tilde{\boldsymbol{q}}(t,\boldsymbol{X}_j)=\boldsymbol{q}_j(t), \qquad \tilde{\boldsymbol{v}}(t,\tilde{\boldsymbol{q}}(t,\boldsymbol{X}_j))=\boldsymbol{v}_j(t).$$

Then we can rewrite (5.1) as

$$\overline{g}^{\eta}=\frac{1}{|\Omega|}\sum_{j=1}^{N}\frac{|\Omega|}{N}g\left(\tilde{\boldsymbol{v}}\left(t,\tilde{\boldsymbol{q}}(t,\boldsymbol{X}_j)\right),\tilde{\boldsymbol{q}}(t,\boldsymbol{X}_j\right)\psi_{\eta}(\boldsymbol{x}-\tilde{\boldsymbol{q}}(t,\boldsymbol{X}_j)), \tag{5.2}$$

where $|\Omega|$ denotes the volume (Lebesgue measure) of Ω. Eq. (5.2) is a Riemann sum generated by partitioning Ω into N cells of volume $|\Omega|/N$ centered at $\boldsymbol{X}_j$. This yields

$$\overline{g}^{\eta}=\frac{1}{|\Omega|}\int_{\Omega}g\left(\tilde{\boldsymbol{v}}(t,\tilde{\boldsymbol{q}}(t,\boldsymbol{X})),\tilde{\boldsymbol{q}}(t,\boldsymbol{X})\right)\psi_{\eta}(\boldsymbol{x}-\tilde{\boldsymbol{q}}(t,\boldsymbol{X}))d\boldsymbol{X}, \tag{5.3}$$

up to discretization error. Now suppose that the map $\tilde{\boldsymbol{q}}(\cdot,\boldsymbol{X})$ is invertible for each t, that is $\boldsymbol{X}=\tilde{\boldsymbol{q}}^{-1}(t,\tilde{\boldsymbol{q}})$. Changing the variables in the integral $\boldsymbol{y}=\tilde{\boldsymbol{q}}(t,\boldsymbol{X})$ we obtain a generic integral approximation

$$\overline{g}^{\eta}=\frac{1}{|\Omega|}\int_{\Omega}g\left(\tilde{\boldsymbol{v}}(t,\boldsymbol{y}),\boldsymbol{y}\right)\psi_{\eta}(\boldsymbol{x}-\boldsymbol{y})J(t,\boldsymbol{y})\ d\boldsymbol{y}, \tag{5.4}$$

where

$$J=|\det\nabla\tilde{\boldsymbol{q}}^{-1}|, \tag{5.5}$$

up to discretization error. For reader's convenience, we list the integral approximations of the average density and momentum,

$$\begin{aligned}\overline{\rho}^{\eta}(t,\boldsymbol{x})&=\frac{M}{N}\sum_{i=1}^{N}\psi_{\eta}(\boldsymbol{x}-\boldsymbol{q}_i(t))\\&=\frac{M}{|\Omega|}\int_{\Omega}\psi_{\eta}(\boldsymbol{x}-\tilde{\boldsymbol{q}}(t,\boldsymbol{X}))d\boldsymbol{X}\\&=\frac{M}{|\Omega|}\int_{\Omega}\psi_{\eta}(\boldsymbol{x}-\boldsymbol{y})J(t,\boldsymbol{y})d\boldsymbol{y}.\end{aligned} \tag{5.6}$$

$$\begin{aligned}\overline{\rho}^{\eta}\overline{\boldsymbol{v}}^{\eta}(t,\boldsymbol{x})&=\frac{M}{N}\sum_{i=1}^{N}\boldsymbol{v}_i(t)\psi_{\eta}(\boldsymbol{x}-\boldsymbol{q}_i(t))\\&=\frac{M}{|\Omega|}\int_{\Omega}\tilde{\boldsymbol{v}}(t,\tilde{\boldsymbol{q}}(t,\boldsymbol{X}))\psi_{\eta}(\boldsymbol{x}-\tilde{\boldsymbol{q}}(t,\boldsymbol{X}))d\boldsymbol{X}\\&=\frac{M}{|\Omega|}\int_{\Omega}\psi_{\eta}(\boldsymbol{x}-\boldsymbol{y})\tilde{\boldsymbol{v}}(t,\boldsymbol{y})J(t,\boldsymbol{y})d\boldsymbol{y}.\end{aligned} \tag{5.7}$$

Here we assumed that all particles have the same mass, $m_i=\frac{M}{N}$.

Note that the $\boldsymbol{y}$-integrals in (5.6) and (5.7) have linear convolution structure. We also point out that these equations are exact provided the interpolants are piecewise linear. In that case, the discrete sums are exact integral quadratures.

The linear averages have a simple relationship between the sums such as (4.9), and the integrals, at least for structured meshes. Another important remark is that for incompressible flows, the microscale Jacobian J is constant. Therefore, the integrals approximations of non-linear averages such as (5.6) and (5.7) become linear. This greatly simplifies calculations and analysis of Lagrangian discretizations of incompressible flows. In particular (5.6) implies that

$$\overline{\rho}^{\eta} = \frac{M}{|\Omega|}, \tag{5.8}$$

if we neglect small variations near the boundary due to the truncation of the kernel ψ_η. The integral approximation for meso-scale momentum reduces to

$$\overline{\boldsymbol{v}}^{\eta}(\boldsymbol{x}) = \int_{\Omega} \tilde{\boldsymbol{v}}(\boldsymbol{y})\psi_\eta(\boldsymbol{x}-\boldsymbol{y})d\boldsymbol{y}. \tag{5.9}$$

The convective stress tensor has an integral approximation

$$\boldsymbol{T}^{\eta}_{(c)}(\boldsymbol{x}) = \overline{\rho}^{\eta} \int_{\Omega} (\overline{\boldsymbol{v}}^{\eta}(\boldsymbol{x}) - \tilde{\boldsymbol{v}}(\boldsymbol{y})) \otimes (\overline{\boldsymbol{v}}^{\eta}(\boldsymbol{x}) - \tilde{\boldsymbol{v}}(\boldsymbol{y}))\psi_\eta(\boldsymbol{x}-\boldsymbol{y})d\boldsymbol{y}, \tag{5.10}$$

and the the interaction stress can be written as:

$$\boldsymbol{T}^{\eta}_{(int)}(\boldsymbol{x}) = \frac{1}{2}\int_{\Omega}\int_{\Omega} \boldsymbol{f}_{int}(\tilde{\boldsymbol{v}}, \boldsymbol{y}, \boldsymbol{y}') \otimes (\boldsymbol{y}'-\boldsymbol{y}) \int_0^1 \psi_\eta\left(s(\boldsymbol{x}-\boldsymbol{y}') + (1-s)(\boldsymbol{x}-\boldsymbol{y})\right) ds d\boldsymbol{y} d\boldsymbol{y}', \tag{5.11}$$

where $\boldsymbol{f}_{int}$ is an interpolant of the pair interaction forces $\boldsymbol{f}_{ij}$.

6. Closure.

6.1. Closure via regularized deconvolution. Our closure construction is based on a simple idea: the integral approximations of the averages are related to the corresponding microscopic quantities via convolutions with ψ_η. These convolutions relate the density and momentum with certain microscopic quantities. Therefore, taking the values of the average density and momentum provided by the meso-scale solver, we can approximate the microscopic quantities by numerically inverting convolution operators. The results are inserted into equations for fluxe(s), such as stress in the momentum balance. This yields closed form equations for primary variables that can be efficiently simulated on coarse space-time grids. In the remainder of the paper, closure is obtained by replacing $\tilde{\boldsymbol{v}}$ in (5.10), (5.11) with its deconvolution approximation.

Define an operator R_η by

$$R_\eta[f](\boldsymbol{x}) = \int \psi_\eta(\boldsymbol{x}-\boldsymbol{y})f(\boldsymbol{y})d\boldsymbol{y},$$

It is easy to check (using Fourier transform, for example) that R_η with a Gaussian kernel is injective. Thus there exists a single-valued inverse operator R_η^{-1}, that we call the *deconvolution operator*. Since the direct operator is compact in $L^2(\Omega)$, the inverse R_η^{-1} is unbounded. Therefore, the inversion problem is ill-posed. This means that small perturbations of the right hand side may lead to large perturbations of the solution. Ill-posed problems are well investigated both analytically and numerically (see, e. g. [9, 11, 16, 23, 3, 38]). The main idea is to approximate the exact inverse by a bounded operator Q. Usually, this approximation depends on a *regularization parameter*. Changing the regularization parameter one can make Q closer to R^{-1} (pointwise). At the same time, the norm of Q increases, so the regularized problem becomes less stable. Many regularization methods are currently available: Tikhonov regularization, iterative methods, reproducing kernel methods, maximum entropy method, methods based on filtered singular value decomposition [11] and others.

Since the discretized version of the kernel of R_η is a sparse symmetric matirx, iterative methods such as Landweber iteration [7], [17] can be quite useful, especially if the number of iterations n can be kept low. This number plays the role of a regularization parameter. For small n, an approximate solution is relatively stable but not necessarily accurate. Typically, low n approximations are smoothed-out and low-pass-filtered

compared to the exact solution The successive approximations to the solution of the equation $R_\eta[\tilde{g}] = \overline{g}$ are given by

$$g_n = \sum_{k=0}^{n} (I - R_\eta)^n \overline{g}, \quad g_0 = \overline{g}, \tag{6.1}$$

where I denotes the identity operator. The first three low-order approximations are

$$\tilde{g} \approx \overline{g} \qquad n = 0, \tag{6.2}$$

$$\tilde{g} \approx \overline{g} + (I - R_\eta)[\overline{g}] \qquad n = 1, \tag{6.3}$$

$$\tilde{g} \approx \overline{g} + (I - R_\eta)[\overline{g}] + (I - R_\eta)^2[\overline{g}] n = 2. \tag{6.4}$$

The zero-order approximation of the velocity is

$$\tilde{\boldsymbol{v}}^\varepsilon = \overline{\boldsymbol{v}}^\eta, \tag{6.5}$$

meaning that the microscale velocity is approximated by the average velocity. In practice $\overline{\boldsymbol{v}}^\eta$ is discretized on a coarse mesh, while $\tilde{\boldsymbol{v}}^\varepsilon$ is an fine scale interpolant of the particle velocities. So, (6.5) should be understood as the equality of a fine scale interpolant in the left hand side, and a coarse scale interpolant in the right hand side. When the interpolant of $\overline{\boldsymbol{v}}^\eta$ is piecewise constant, (6.5) implies that all particles located within the averaging volume centered at a coarse grid point should be assigned the average velocity at that grid point. This simple closure is very similar to the Cauchy-Born rule [20] used in quasi-continuum method [21], [34]. In general, the Cauchy-Born rule does not hold even in variational lattice problems [8], but it is a good approximation for many problems of practical interest. In [31] we used zero-order closure with good results for non-linear oscillator chains with "well prepared" initial conditions characterized by small velocity fluctuations. For more general initial conditions, zero-order closure fails, but it is still possible to generate a sufficiently accurate deconvolution closure [30].

7. Examples.

7.1. Non-stationary Poiseuille flow. The non-steady, gravity-driven, zero pressure gradient Poiseuille flow in two dimensions can be modeled by the heat equation

$$\overline{\rho} u_t = \mu u_{yy} + \overline{\rho} g, \quad y \in (0, L). \tag{7.1}$$

where $u(y,t)$ is the x-component of the velocity, x and y are the coordinates in the direction respectively parallel and perpendicular to the axis of the pipe, g is the gravity acceleration, $\overline{\rho}$ is a constant fluid density, and μ is the shear viscosity. Dividing by $\overline{\rho}$ and setting $a^2 = \mu/\overline{\rho}$, we get the classical initial boundary value problem for the heat equation

$$u_t = a^2 u_{yy} + g, \qquad y \in (0, L) \tag{7.2}$$

with zero Dirichlet boundary conditions and some initial conditions. The solution of (7.2) can be represented as $u(y,t) = v_p(y) + v(y,t)$ where $v_p(y)$ is the steady solution of the non-homogeneous equation (this is the classical Poiseuille parabolic velocity profile), and $v(y,t)$ is the solution of the mixed boundary value problem

$$v_t = a^2 v_{yy}, \quad y \in (0, L), \tag{7.3}$$

$$v(0,t) = v(L,t) = 0, \tag{7.4}$$

$$v(y,0) = v_0(y). \tag{7.5}$$

We are interested in oscillatory initial conditions, so we prescribe

$$v_0(y) = \sin \frac{\pi m}{L} y, \tag{7.6}$$

where m is an integer. Using separation of variables, we find the solution of (7.3)-(7.6):

$$v(y,t) = e^{-\lambda_m^2 t} \sin \frac{\pi m}{L} y, \tag{7.7}$$

where

$$\lambda_m = \frac{\pi a m}{L}.$$

This means that, even for m large, choosing a sufficiently small will produce a solution that decreases slowly in time and rapidly oscillates with respect to y. Discretizing (7.7) on the fine scale mesh we obtain a collection of particle velocities

$$v_j(t) = v(y_j, t), \quad j = 1, 2, \ldots, N.$$

In the remainder of this section, we approximate all discrete averages by integrals for simplicity of exposition. Then the average velocity

$$\overline{v}^\eta(y,t) = \frac{1}{\sqrt{\pi}\eta} \int_0^L v(y,t) e^{-\frac{(y-y')^2}{\eta^2}} dy'. \tag{7.8}$$

Changing variable of integration $z = (y - y')/\eta$ and using standard formula for the Fourier transform of Gaussian functions, we see that the average velocity can be well approximated by

$$\overline{v}^\eta(y,t) = R_\eta[v] = e^{-\eta^2 \frac{\pi^2 m^2}{4L^2}} v(y,t). \tag{7.9}$$

Therefore, no matter how small η is, we still can find m large enough so that $|\overline{v}^\eta|$ is much smaller than $|v|$. This produces velocity fluctuations on the order of $|v|$ itself, and for small a, these fluctuations may decay rather slowly as t increases. Another important implication of (7.9) is

$$(I - R_\eta)[\overline{v}^\eta] = \left(1 - e^{-\eta^2 \frac{\pi^2 m^2}{4L^2}}\right) \overline{v}^\eta. \tag{7.10}$$

Therefore, iterative approximations (6.1)) for the velocity, $v_n = \sum_{k=0}^n (I - R_\eta)^k [\overline{v}^\eta]$ can be written as

$$v_n = \overline{v}^\eta \sum_{k=0}^n \left(1 - e^{-\eta^2 \frac{\pi^2 m^2}{4L^2}}\right)^k = \overline{v}^\eta \frac{1 - \left(1 - e^{-\eta^2 \frac{\pi^2 m^2}{4L^2}}\right)^{n+1}}{1 - e^{-\eta^2 \frac{\pi^2 m^2}{4L^2}}}, \tag{7.11}$$

where we used the formula for the sum of the geometric progression. We can also recognize that v_n, up to a factor $\overline{v}^\eta$, are partial sums of the geometric series with ratio $q = \left(1 - e^{-\eta^2 \frac{\pi^2 m^2}{4L^2}}\right) < 1$. Therefore, as $n \to \infty$, v_n converge, uniformly on $(0, L)$, to the sum of the geometric series, $\overline{v}^\eta \frac{1}{1-q}$. Thus

$$\lim_{n\to\infty} v_n = \overline{v}^\eta e^{\eta^2 \frac{\pi^2 m^2}{4L^2}} = e^{-\eta^2 \frac{\pi^2 m^2}{4L^2}} v(y,t) e^{\eta^2 \frac{\pi^2 m^2}{4L^2}} = v(y,t). \tag{7.12}$$

This shows that successive approximations converge to the true microscopic velocity. It is also easy to estimate the speed of convergence:

$$|v_n - v| \le |v| q^{n+1} = |v| \left(1 - e^{-\eta^2 \frac{\pi^2 m^2}{4L^2}}\right)^{n+1} \le e^{-\lambda_m^2 t} \left(1 - e^{-\eta^2 \frac{\pi^2 m^2}{4L^2}}\right)^{n+1}.$$

When $\lambda_m \ll 1$, and $\eta m \gg 1$, convergence is rather slow, since in that case q is close to 1. This also clarifies the role played by the initial conditions. If the initial conditions are slowly varying (contain a few low frequency Fourier modes), then low order closure is reasonably accurate. Higher order approximations are necessary to deal with the high frequency modes in the initial conditions.

The same is true for approximating stresses. To illustrate this, we calculate the convective stress, using the "exact" fine scale velocity $v(y,t)$, and compare with the zero-order closure approximation. The xy-component of the convective stress tensor is

$$T_{(c)}^{exact} = \overline{\rho} \frac{1}{\sqrt{\pi}\eta} \int (\overline{v}^\eta(y,t) - v(y',t))^2 e^{-\frac{(y-y')^2}{\eta^2}} dy'.$$

Since $\overline{v}^\eta \ll v$, the dominant term in the above expression is

$$\overline{\rho}\frac{1}{\sqrt{\pi}\eta}\int v^2(y',t)e^{-\frac{(y-y')^2}{\eta^2}}dy' = \overline{\rho}e^{-2\lambda_m^2 t}\frac{1}{\sqrt{\pi}\eta}\int \sin^2\left(\frac{\pi m}{L}y'\right)e^{-\frac{(y-y')^2}{\eta^2}}dy'$$
$$= \frac{1}{2}\overline{\rho}e^{-2\lambda_m^2 t} - \frac{1}{2}\overline{\rho}e^{-2\lambda_m^2 t}\int \cos\left(\frac{2\pi m}{L}y\right)e^{-\frac{(y-y')^2}{\eta^2}}dy'.$$

Using Fourier transform it is easy to verify that the last integral is small, provided $m\eta \gg 1$. Then

$$T_{(c)}^{exact} \approx \frac{1}{2}\overline{\rho}e^{-2\lambda_m^2 t}.$$

The convective stress corresponding to zero-order closure is

$$T_{(c)}^0 = \overline{\rho}\int(\overline{v}^\eta(y) - \overline{v}^\eta(y'))^2\psi_\eta(y-y')dy' = e^{-2\lambda_m^2 t}e^{-2\eta^2\frac{pi^2m^2}{4L^2}}\int\left(\sin\frac{\pi m}{L}y - \sin\frac{\pi m}{L}y'\right)^2\psi_\eta(y-y')dy'.$$

For large m, $e^{-2\eta^2\frac{pi^2m^2}{4L^2}}$ is small, so that

$$|T_{(c)}^{exact} - T_{(c)}^0| \approx |T_{(c)}^{exact}|,$$

meaning that zero order closure is very crude. For m small enough, $e^{-2\eta^2\frac{\pi^2m^2}{4L^2}}$ is close to one, and the error is much smaller.

Next we consider the xy-component $T_{(int)}^\eta$ of the interaction stress, given by (4.7). Assuming that the interaction forces $\boldsymbol{f}_{jk}$ are defined by (3.5) (these forces are linear functions of the relative velocities), and using (7.7) for $v(y,t)$ and (7.9) for $\overline{v}^\eta$ we obtain

$$T_{(int)}^0 = e^{-\eta^2\frac{\pi^2m^2}{4L^2}}T_{(int)}^{exact},$$

where T^0 correspond to the zero-order closure approximation obtained by replacing v with $\overline{v}^\eta$ in (4.7). If $\eta m \gg 1$, $|T_{(int)}^0| \ll |T_{(int)}^{exact}$, which yields a nearly 100% error in approximating interaction stress. More generally, we can evaluate higher order approximations $T_{(int)}^n$ by using v_n from (7.11) in (4.7):

$$T_{(int)}^n = \left(1 - \left(1 - e^{-\eta^2\frac{\pi^2m^2}{4L^2}}\right)^{n+1}\right)T_{(int)}^{exact}. \tag{7.13}$$

Thus $T_{(int)}^n$ converges to $T_{(int)}^{exact}$ as $n \to \infty$. In addition, Eq. (7.13) can be used to determine the order n of the approximation needed to achieve desired tolerance in approximating stresses induced by a particular Fourier mode with a given value of m.

To summarize, this example shows that iterative closure performs better if the initial conditions do not contain higher frequency harmonics. For such initial conditions, low order approximations, even zero-order closure, can be expected to perform reasonably well. Another conclusion is that the parameter ηm determines the accuracy of approximation. This can be used to determine the resolution η needed to achieve a desired tolerance with given initial conditions and a specified value of n.

7.2. Pipe flow with periodic microstructure. Here we consider a two-dimensional Poiseuille-type flow of the fluid with variable viscosity μ^δ that is constant in the x-direction and varies rapidly in the y-direction:

$$\mu^\delta(y) = \mu\left(\frac{y}{\delta}\right), \qquad \mu(y) = \frac{1}{1 - \frac{2\pi b}{L}\sin\left(\frac{2\pi}{L}y\right)}, \tag{7.14}$$

where $\delta \ll 1$. The constant b should be such that

$$0 < \frac{2\pi b}{L} < 1,$$

to ensure that μ^δ is bounded from below uniformly in δ.

The flow velocity $u^\delta(t,y)$ satisfies the heat equation

$$\overline{\rho} u_t^\delta = \partial_y \left(\mu^\delta(y) \partial_y u_y^\delta \right) + \overline{\rho} g, \quad y \in (0, L). \tag{7.15}$$

with periodic boundary conditions. Direct calculation yields a steady-state solution satisfying zero boundary conditions:

$$u_p^\delta = -\frac{1}{2}\rho g y^2 + Ay + \frac{B\cos Dy}{D}(A - \rho g y) + \frac{B}{D^2}\rho g \sin Dy + C, \tag{7.16}$$

where

$$B = \frac{2\pi b}{L}, \qquad D = \frac{2\pi}{\delta L},$$

and the constants of integration are

$$A = \rho g \frac{\frac{1}{2}L^2 + L\frac{B}{D}\cos\left(\frac{2\pi}{\delta}\right) - \frac{B}{D^2}\sin\left(\frac{2\pi}{\delta}\right)}{L + \frac{B}{D}\cos\left(\frac{2\pi}{\delta}\right) - \frac{B}{D}} \tag{7.17}$$

and

$$C = -\frac{B}{D}A \tag{7.18}$$

For a constant viscosity, the first two terms in (7.16) give to the classical Poiseuille profile, while the other terms are due entirely to the variations in viscosity. Writing $u^\delta = u_p^\delta + v^\delta$, we see that v^δ satisfies

$$\overline{\rho} v_t^\delta = \partial_y \left(\mu^\delta(y) \partial_y v_y^\delta \right) \quad y \in (0, L). \tag{7.19}$$

with periodic boundary conditions. The initial condition is given by (7.6). Homogenization theory for parabolic equations [13] gives an asymptotic approximation of v^δ:

$$v^\delta \approx v^0(t,y) + \delta w\left(\frac{y}{\delta}\right)\partial_y v^0, \tag{7.20}$$

where v^0 solves the effective equation

$$\overline{\rho} v_t^0 = \mu^\star v_y^0 y \tag{7.21}$$

with the constant effective viscosity $\mu^\star$ and $w(y)$ is an L-periodic function with zero average on $(0, L)$ that solves the so-called cell problem

$$(\mu(y)(1 + w'(y)))' = 0, \qquad \text{on } (0, L), \tag{7.22}$$

Once (7.22) is solved, the effective viscosity can be determined from

$$\mu^\star = \frac{1}{L}\int_0^L \mu(y)(1 + w'(y))dy. \tag{7.23}$$

Direct calculation shows that

$$w(y) = b\cos\left(\frac{2\pi}{L}y\right). \tag{7.24}$$

and

$$\mu^\star = 1.$$

Solving the effective equation by separation of variables yields

$$v^0 = e^{-\lambda_m^2 t} \sin\left(\frac{\pi m y}{L}\right).$$

with

$$\lambda_m = \frac{\pi m}{\sqrt{\overline{\rho}} L}.$$

Substituting this and (7.24) into (7.20) and using standard trigonometric identity we have

$$v^\delta = e^{-\lambda_m^2 t}\left(\sin\left(\frac{\pi m y}{L}\right) + \frac{1}{2}\delta\frac{\pi m b}{L}\cos\left(\frac{\pi y}{L}(\frac{2}{\delta}+m)\right) + \frac{1}{2}\delta\frac{\pi m b}{L}\cos\left(\frac{\pi y}{L}(\frac{2}{\delta}-m)\right)\right). \tag{7.25}$$

up to the terms of higher order in δ. The fluid stress on the microscale is determined by the flux

$$\begin{aligned}\mu^\delta(y)\partial_y v^\delta &= \mu^\delta(y)\left(1 + w'\left(\frac{y}{\delta}\right)\right)\partial_y v^0 + \delta\mu^\delta(y) w\left(\frac{y}{\delta}\right)\partial_{yy}^2 v^0 \\ &= \partial_y v^0 + \delta\mu^\delta(y) w\left(\frac{y}{\delta}\right)\partial_{yy}^2 v^0 \\ &= \frac{\pi m}{L} e^{-\lambda_m^2 t}\cos\frac{\pi m y}{L} - \delta\left(\frac{\pi m}{L}\right)^2 e^{-\lambda_m^2 t}\frac{b\cos\frac{2\pi y}{\delta L}\sin\frac{\pi m y}{L}}{1-\frac{2\pi b}{L}\sin\frac{2\pi y}{\delta L}}.\end{aligned} \tag{7.26}$$

The average velocity corresponding to (7.25) is

$$\begin{aligned}\overline{v}^\delta &= e^{-\lambda_m^2 t} e^{-\frac{(\eta\pi m)^2}{4L^2}}\sin\left(\frac{\pi m y}{L}\right) \\ &+ \frac{1}{2}\delta\frac{\pi m b}{L} e^{-\lambda_m^2 t} e^{-\frac{\eta^2\pi^2}{4L^2}(2\delta^{-1}+m)^2}\cos\left(\frac{\pi y}{L}(2\delta^{-1}+m)\right) \\ &+ \frac{1}{2}\delta\frac{\pi m b}{L} e^{-\lambda_m^2 t} e^{-\frac{\eta^2\pi^2}{4L^2}(2\delta^{-1}-m)^2}\cos\left(\frac{\pi y}{L}(2\delta^{-1}-m)\right).\end{aligned} \tag{7.27}$$

The nth order Landweber approximation v_n^δ of the exact velocity v^δ is

$$\begin{aligned}v_n^\delta &= e^{-\lambda_m^2 t}\frac{1-q_1^{n+1}}{1-q_1} e^{-\frac{(\eta\pi m)^2}{4L^2}}\sin\left(\frac{\pi m y}{L}\right) \\ &+ \frac{1}{2}\delta\frac{\pi m b}{L} e^{-\lambda_m^2 t}\frac{1-q_2^{n+1}}{1-q_2} e^{-\frac{\eta^2\pi^2}{4L^2}(2\delta^{-1}+m)^2}\cos\left(\frac{\pi y}{L}(2\delta^{-1}+m)\right) \\ &+ \frac{1}{2}\delta\frac{\pi m b}{L} e^{-\lambda_m^2 t}\frac{1-q_3^{n+1}}{1-q_3} e^{-\frac{\eta^2\pi^2}{4L^2}(2\delta^{-1}-m)^2}\cos\left(\frac{\pi y}{L}(2\delta^{-1}-m)\right),\end{aligned} \tag{7.28}$$

where

$$\begin{aligned}q_1 &= 1 - e^{-\eta^2 m^2 k^2}, \\ q_2 &= 1 - e^{-\eta^2(2\delta^{-1}+m)^2 k^2}, \\ q_2 &= 1 - e^{-\eta^2(2\delta^{-1}-m)^2 k^2},\end{aligned} \tag{7.29}$$

and

$$k = \frac{\pi}{2L}.$$

The coefficients q_j determine the speed of convergence of terms in (7.28) to the corresponding terms in (7.25). Since q_2 and q_3 are much closer to 1 than q_1, the convergence speed of the first term is much faster than the second and third terms. In practice it would take many more iterations to reconstruct the high frequency

components than the low frequency component. As the number of iterations increaseas, instability of the problem becomes more pronounced, and high frequency content of the solution may be lost in the noise.

Stability of the reconstruction can be improved by filtering. Construction of the filter is based on the use of a priori information about the solution. For low frequency initial conditions, the spectrum of the microscale velocity contains two well separated bands: the low frequency band determined by the initial conditions, and the high frequency band determined by the interaction forces. The central frequency of the latter is on the order of δ^{-1} (it is $2/\delta$ in our example), and the band width is roughly twice that of the low frequency band. Moreover, each low frequency mode gives rise to two high frequency modes. Define a filter acting on the average velocity as follows. The low frequency mode is left unchanged, and each high frequency mode is multiplied by a factor $e^{\eta^2\nu^2k^2-\alpha\eta^2m^2k^2}$, where ν is the mode frequency, and $\alpha \geq 1$ is a parameter added to improve stability of the filter. Adding a stabilizing factor makes sense because of the presence of errors. This factor prevents the filtered Fourier coefficients from increasing with frequency, which could completely destabilize computations.

After filtering the average velocity $\overline{v}^\delta$ in (7.27) we obtain a modified velocity $\tilde{v}^\delta$ defined by

$$\begin{aligned}\mathcal{F}\overline{v}^\delta = \tilde{v}^\delta = e^{-\lambda_m^2 t}e^{-\eta^2m^2k^2}\sin\Big(\frac{\pi my}{L}\Big) + \frac{1}{2}\delta\frac{\pi mb}{L}e^{-\lambda_m^2 t}e^{-\alpha\eta^2m^2k^2}\cos\Big(\frac{\pi y}{L}(2\delta^{-1}+m)\Big) \\ + \frac{1}{2}\delta\frac{\pi mb}{L}e^{-\lambda_m^2 t}e^{-\alpha\eta^2m^2k^2}\cos\Big(\frac{\pi y}{L}(2\delta^{-1}-m)\Big).\end{aligned} \tag{7.30}$$

Applying the filtering operator $\mathcal{F}$ to the both sides of the equation $R_\eta[v^\delta] = \overline{v}^\eta$ and then iterating as before yields successive approximations

$$\begin{aligned}\tilde{v}_n^\delta = e^{-\lambda_m^2 t}e^{-\eta^2m^2k^2}\frac{1-q_1^{n+1}}{1-q_1}\sin\Big(\frac{\pi my}{L}\Big) \\ + \frac{1}{2}\delta\frac{\pi mb}{L}e^{-\lambda_m^2 t}e^{-\alpha\eta^2m^2k^2}\frac{1-q_4^{n+1}}{1-q_4}\cos\Big(\frac{\pi y}{L}(2\delta^{-1}+m)\Big) \\ + \frac{1}{2}\delta\frac{\pi mb}{L}e^{-\lambda_m^2 t}e^{-\alpha\eta^2m^2k^2}\frac{1-q_4^{n+1}}{1-q_4}\cos\Big(\frac{\pi y}{L}(2\delta^{-1}-m)\Big),\end{aligned} \tag{7.31}$$

where q_1 is defined in (7.29), and

$$q_4 = 1 - e^{-\alpha\eta^2m^2k^2},$$

Now the rate of convergence of all three terms is determined by the frequency content of the initial conditions.

Next, a straightforward calculation yields an approximate flux $\mu^\delta\partial_y\tilde{v}_n^\delta$ that we can compare with the exact micro-scale flux $\mu^\delta\partial_y v^\delta$ defined in (7.26). To make comparison easier we write $\mu^\delta\partial_y\tilde{v}_n^\delta$ in the form

$$\begin{aligned}\mu^\delta\partial_y\tilde{v}_n^\delta = \frac{\pi m}{L}e^{-\lambda_m^2 t}(1-q_1^{n+1})\cos\frac{\pi my}{L} \\ - \frac{2\pi^2mb}{L^2}e^{-\lambda_m^2 t}(q_1^{n+1}-q_4^{n+1})\frac{\sin\frac{2\pi y}{\delta L}\cos\frac{\pi my}{L}}{1-\frac{2\pi b}{L}\sin\frac{2\pi y}{\delta L}} \\ - \delta\frac{\pi^2m^2b}{L^2}(1-q_4^{n+1})\frac{\cos\frac{2\pi y}{\delta L}\sin\frac{\pi my}{L}}{1-\frac{2\pi b}{L}\sin\frac{2\pi y}{\delta L}},\end{aligned} \tag{7.32}$$

As $n \to \infty$, the first and third terms terms converge to, respectively, the first and second terms in (7.26), while the second term converges to zero.

The important feature of this example is the highly non-uniform nature of the interaction forces. This leads to a special type of dynamics, where slowly oscillating initial conditions produce rapidly oscillating solutions. For such systems, high frequency oscillations cannot be simply filtered out, because they contain essential information about the dynamics of mesoscale averages. Specifically, the flux $\mu^\delta\partial_y v^\delta$ in (7.26) cannot be adequately described by the average velocity alone. In addition, one needs the corrector w that encodes the influence of the high frequency content of the velocity on the low-frequency content of the flux.

The example of this section shows that deconvolution closure augmented by filtering can reproduce the main result of the periodic homogenization method: the effective flux approximation. The filtering amounts to boosting high frequency component of the solution while leaving the low frequency components intact. This has to be done carefully because of stability requirements. However, one can always design an effective filter provided the singular value system for R_η is available. Since this operator is independent of dynamics, the singular values and vectors can be pre-computed and then used repeatedly for many different ODE systems. In Fig. 7.1 we show the approximate microscale velocity profiles computed from (7.31) at different

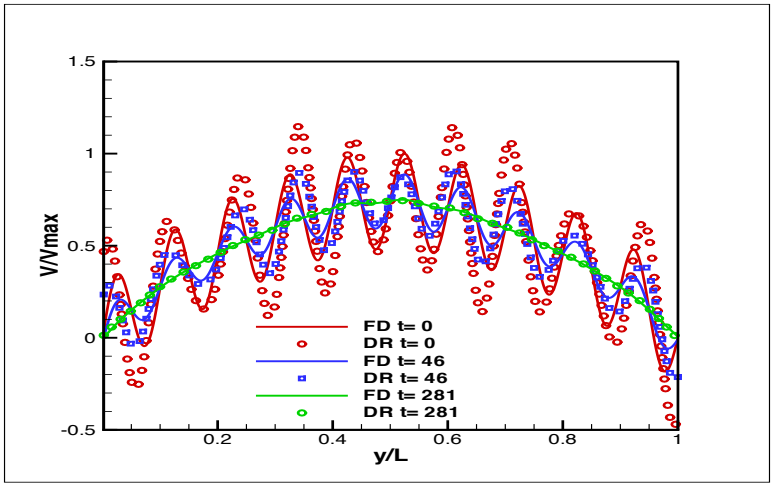

FIG. 7.1.

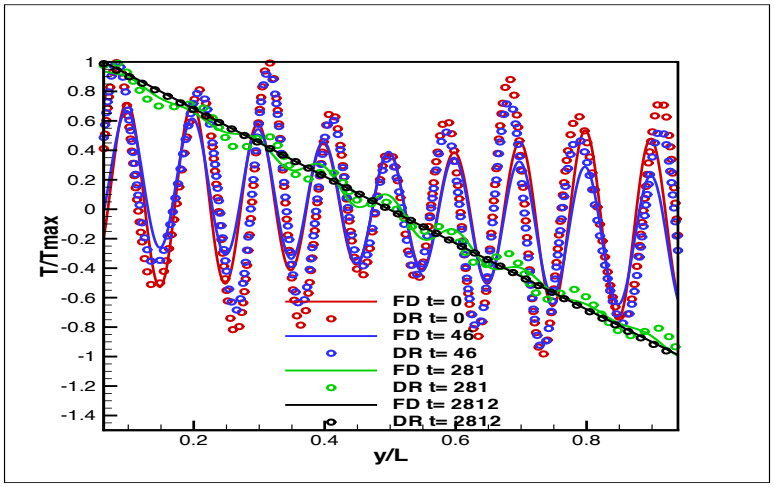

FIG. 7.2.

times (annotated as DR for "dimension reduction"). These approximations are compared to the velocity from the finite-difference direct simulation (marked FD). The Fig. 7.2 shows the average stress calculated by applying spatial averaging to the flux in (7.32) (annotated as DR), and the average stress computed from direct simulation (FD). In both figures, $n = 1000$, $\varepsilon = 1/512$, and $\delta = 2/3$, $b = \frac{L}{8\pi}$, $L = 128$, $m = 20$.

8. Non-newtonian two-fluid flow. In this section, we consider a two-dimensional layered flow of a fluid-fluid mixture in a channel of the uniform width $L = 128$. On the boundary of the channel, the velocity is prescribed to be zero. The initial velocity is zero as well. The objective is to simulate the evolution of velocity to a steady state. The layers are oriented parallel to the walls of the channel and have different sizes

(widths). The geometric distribution of layers is non-uniform and is shown in Fig 8.1. In both phases we use Newtonian constitutive laws with constant viscosities $\mu_1 = 100$ and $\mu_2 = 200$. Density of both fluids are taken to be the same. We assume that such flow can be accurately described by an SPH lagrangian particle model. The details of the SPH model are given in [35]. In this model, interaction force $\boldsymbol{f}_{ij}$ for isothermal low-Reynolds number flow of Newtonian fluids with non-uniform viscosity is given by:

$$\boldsymbol{f}_{ij} = -\left(\frac{P_j}{n_j^2} + \frac{P_i}{n_i^2}\right)\nabla_i w(\boldsymbol{q}_i - \boldsymbol{q}_j) + \frac{4\mu_i\mu_j}{\mu_i + \mu_j}\frac{\boldsymbol{v}_i - \boldsymbol{v}_j}{n_i n_j |\boldsymbol{q}_i - \boldsymbol{q}_j|^2}(\boldsymbol{q}_i - \boldsymbol{q}_j)\cdot\nabla_i w(\boldsymbol{q}_i - \boldsymbol{q}_j). \tag{8.1}$$

Here, $\boldsymbol{q}_i(t)$ are particle positions, $\boldsymbol{v}_i(t)$ are velocities, μ is the fluid viscosity, w is the SPH weighting function with compact support h that is on the order of ε. We use a fourth-order weighting function w with [37]:

$$w(\mathbf{r}) = \beta\begin{cases} \left(3 - \frac{3|\mathbf{r}|}{h}\right)^5 - 6\left(2 - \frac{3|\mathbf{r}|}{h}\right)^5 + 15\left(1 - \frac{3|\mathbf{r}|}{h}\right)^5 & \text{if} \quad 0 \le |\mathbf{r}| < h/3, \\ \left(3 - \frac{3|\mathbf{r}|}{h}\right)^5 - 6\left(2 - \frac{3|\mathbf{r}|}{h}\right)^5 & \text{if} \quad h/3 \le |\mathbf{r}| < 2h/3. \\ \left(3 - \frac{3|\mathbf{r}|}{h}\right)^5 & \text{if} \quad 2h/3 \le |\mathbf{r}| < h, \\ 0 & \text{if} \quad |\mathbf{r}| > h. \end{cases} \tag{8.2}$$

where

$$h = 4\Delta, \qquad \Delta = L/512 = 0.25, \tag{8.3}$$

(Δ denotes the fine grid step size). Further, the normalization constant $\beta = \frac{63}{478\pi h^2}$ ($\beta = \frac{81}{359\pi h^3}$) in two (three) spatial dimensions. Particle density n_i is found as

$$n_i = \sum_j w\left(\boldsymbol{q}_i - \boldsymbol{q}_j\right). \tag{8.4}$$

Each fluid is represented by its own fixed set of particles. For immiscible multiphase fluid systems, van der Waals equation of state can be used to close the SPH equations [35]:

$$P_i = \frac{n_i k_B T}{1 - c_1 n_i} - k_{ij} c_2 n_i^2. \tag{8.5}$$

In this equation of state, k_B is the Boltzman constant, T is the temperature (assumed here to be constant), and c_1 and c_2 are the van der Waals constants (assumed here to be the same for all fluids). The parameter k_{ij} is set to 1 when interacting particles i and j are of the same fluid and to $k^* < 1$ for interaction between particles of different fluids. The surface tension between two fluids increases with decreasing k^*. In our simulations, the surface tension stabilizes the flow by preventing development of the Kelvin-Helmholtz instability.

In the microscopic model, we assume that positions $\boldsymbol{q}_i$ lie on a periodic mesh with grid size Δ defined in (8.3). For the meso-scale model, we chose the resolution parameter $\eta = 0.04$. The corresponding meso-scale mesh has the mesoscale grid size $\Delta_\eta = 4$. The smallest width of the layers is about 1 and the largest width of the layers is 16, so the layers span all scales from the macroscopic to microscopic. We simulated the reduced model by numerically solving the momentum balance equation (4.5). For the stress approximation we used the the second-order Landweber approximation for the micro-scale velocities. The average velocity computed by the meso-solver was then compared with the average velocity generated by the direct solution of the SPH equations. Fig. 8.1 shows that the meso-scale solution agrees quite well with the direct simulation.

Let us now estimate the computational savings for this example. In the direct SPH simulations, the operation count per time step is proportional to $N \times N_b$, where N is the number of particles and

$$N_b = \pi h^2 \frac{1}{\Delta^2} = 16\pi$$

is approximately equal to the number of particles within distance h from each particle. Consequently, the operation count of per time step of the direct simulations scales as $O(N)$ as $N \to \infty$. In the meso-scale simulation, we solve equation (4.5) on the coarse mesh with the grid size η. We use explicit time integration, and the operation count for integration the meso-scale equations is proportional to the number of nodes in the coarse mesh, N_η, that is independent of the number of particles. In the solution presented here

$$N/N_\eta = 256.$$

The reconstruction of the micro-scale velocities and calculation of the meso-scale stresses also adds to the total operation count of the meso-solver, especially estimation of $\boldsymbol{T}^\eta_{int}$ that involves double summation or double integration. Here we use a coarse-fine approximation of the integral expression for $\boldsymbol{T}^\eta_{int}$ [36]. To make the presentation self-contained, we provide a brief description of this approximation here. First, using (8.1) in the integral approximation (5.11), and making the change of variables $\boldsymbol{R} = \frac{1}{2}(\boldsymbol{y} + \boldsymbol{y}')$, $\boldsymbol{\rho} = \boldsymbol{y} - \boldsymbol{y}'$, we obtain

$$\overline{T}^\eta_{int}(t, \boldsymbol{x}) \approx \int_\Omega \int_{D_w} \bar{\boldsymbol{f}}(t, \boldsymbol{R}, \boldsymbol{\rho}) \otimes \boldsymbol{\rho} \int_0^1 \psi_\eta \left(\boldsymbol{x} - \boldsymbol{R} + (s - 1/2)\boldsymbol{\rho}\right) ds \; d\boldsymbol{\rho} \; d\boldsymbol{R}, \tag{8.6}$$

where

$$\begin{aligned} \bar{\boldsymbol{f}}(t, \boldsymbol{R}, \boldsymbol{\rho}) = &- \left(\frac{P}{n^2}(t, \boldsymbol{R} + \boldsymbol{\rho}/2) + \frac{P}{n^2}(t, \boldsymbol{R} - \boldsymbol{\rho}/2) \right) \nabla w(\boldsymbol{\rho}) \\ &+ \frac{4\mu_1\mu_2}{\mu_1 + \mu_2} \frac{(\tilde{\boldsymbol{v}}(t, \boldsymbol{R} + \rho/2) - \tilde{\boldsymbol{v}}(t, \boldsymbol{R} - \boldsymbol{\rho}/2))}{n\,(t, \boldsymbol{R} + \boldsymbol{\rho}/2)\, n\,(t, \boldsymbol{R} - \boldsymbol{\rho}/2)} \frac{\boldsymbol{\rho}}{|\boldsymbol{\rho}|^2} \cdot \nabla w(\boldsymbol{\rho}). \end{aligned} \tag{8.7}$$

In (8.6), the integration with respect to $\boldsymbol{\rho}$ is over D_w, the support of the micro-scale window function w. Next, observe that P, n, and ψ_η are slowly varying (in space) functions, and $\tilde{\boldsymbol{v}}$ is approximated by the low-order deconvolution that is slowly varying as well. This suggests that the integral with respect to $\boldsymbol{R}$ can be discretized on the coarse mesh with about N_η points. The $\boldsymbol{\rho}$-integral is discretized on a fine mesh, but because of the smallness of the domain of integration, the number of mesh points needed for this dicretization is about N_b (independent of N). In the example presented here, we used a coarse mesh with

$$N_C = 4N_\eta$$

mesh points for $\boldsymbol{R}$-integral discretization, and the standard fine mesh with grid-size Δ for the $\boldsymbol{\rho}$-integral. The operation count associated with calculation of $\boldsymbol{T}^\eta_{int}$ is proportional to $4N_\eta \times N_b = 64\pi N_\eta$.

The coarse-fine discretization also suggests an efficient interpolation procedure for the reconstructed velocity. In the meso-scale simulation, the second-order Landweber approximation is computed on the coarse mesh, and then interpolated to the fine mesh. Equations (8.6) and (8.7) make it clear that for each coarse mesh point $\boldsymbol{R}_j$ we only need to evaluate this interpolant at the fine mesh points $\boldsymbol{R}_j \pm \boldsymbol{\rho}_k/2$, where $\boldsymbol{\rho}_k/2$ should be within the support of the function w in (8.2) shifted by $\boldsymbol{R}_j$. In other words, for each j, we only need $\boldsymbol{\rho}_k$ such that

$$\left| \boldsymbol{R}_j \pm \frac{1}{2}\boldsymbol{\rho}_k \right| \leq h.$$

The number of these points is about N_b. In view of the above, the operation count for the deconvolution-interpolation is about $4N_\eta \times N_b$, provided that piecewise linear interpolation is used.

Another task is calculation of the integral approximation of the convective stress $\boldsymbol{T}^\eta_c$ defined by (5.10). Since $\overline{\boldsymbol{v}}, \psi_\eta$ are coarse scale quantities, and $\tilde{\boldsymbol{v}}$ is approximated by the coarse second-order deconvolution, the integral is discretized on a coarse mesh with N_η points. The associated computational cost is proportional to N_η.

Adding up the above estimates we find that the total operation count per time step of the meso-solver is about

$$2N_\eta + 8N_\eta \times N_b = (2 + 128\pi)N_\eta, \tag{8.8}$$

(about N_η flops for the update step, N_η flops for calculating the convective stress, and $4N_\eta \times N_b$ each for computing deconvolution-interpolation and interactive stress).

Estimate (8.8) implies that the operation count per time step scales as $O(1)$ as $N \to \infty$. The operation count depends on η and other parameters of the problems, but not on N. For large N, this offers a significant advantage over direct simulation.

Furthermore, the time step in the direct simulation should be smaller than $\Delta^2\rho/\mu$, while in the meso-scale simulation the time step should be less than $\eta L/v_{max}$ (v_{max} is the maximum fluid velocity). In the example presented here, the meso-solver time step is approximately 32 times larger then the time step in the direct simulation.

In contrast to the periodic flow example, no filtering was used. The simulation results suggest that deconvolution closure is better suited for problems without strong scale separation. Therefore, our method can be viewed as complementary to many existing techniques in homogenization of PDEs and ODEs.

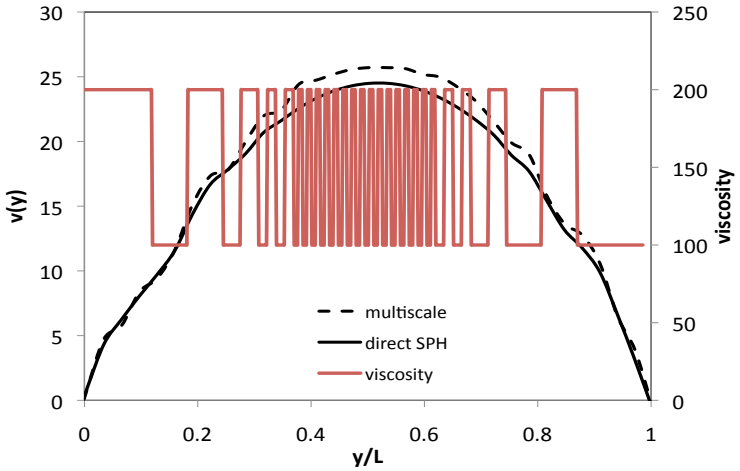

FIG. 8.1. *Comparison of the steady-state average velocity obtained from the meso-scale simulation with the same quantity computed by direct fine scale simulation. Viscosity distribution is given by the red line. Zero initial conditions were used for both meso-scale and fine scale simulations.*

9. Conclusions. In this paper, we develop a model reduction method for large ODE systems modeling the flow of one- and two-phase fluids, including fluids with microstructure. The method applies when the primarily object of interest are spatial averages, specifically average density and velocity. Such averages satisfy the exact balance equations, but the fluxes in these equations depend on the micro-scale velocities. The main ingredient of the method, deconvolution-based closure from [31], [30], [36], generates approximate fluxes that depend only on the average density and velocity. Such approximations can be evaluated without solving the fine scale problem. This provides complexity reduction and produces computational savings. We extend and clarify the approach developed in [36], and analyze convergence of the method in a simple example of two-dimensional pipe flow of a homogeneous fluid. We also consider an example of a two-fluid flow with a periodic viscosity exhibiting high frequency oscillations and show that the deconvolution closure, augmented by filtering, leads to essentially the same results as classical homogenization. Finally, we provide an example of a complete meso-scale simulation. The model again is a two-fluid layered flow in a channel, but the layers have variable widths. The size of the layers varies between macro-and micro-scales. Homogenization applies in principle, but the effective viscosity is much harder to calculate than in the periodic case. Our method produces good agreement between the average velocity simulated by the meso-solver and the average velocity obtained from direct simulation. The operation count per time step of the meso-scale simulation is independent of N (the number of particles in the fine scale simulation) while direct simulation requires $O(N)$ flops per time step. The time step in the meso-solver is about 32 times larger than the time step in the direct simulation. This example demonstrates potential usefulness of the deconvolution closure for efficient

simulation of of multiphase mixtures.

REFERENCES

[1] Adams, N. A., and Stolz, S. A subgrid-scale deconvolution approach for shock capturing. *J. Comp. Phys.*, 178, 2 (2002), 391-426.

[2] Bercelli, L.C., Iliescu T., and Layton W. J. *Mathematics of large eddy simulation of turbulent flows.* Springer, NY, 2006.

[3] Engl H. W. , Hanke M. , and Neubauer A. *Regularization of Inverse Problems.* Kluwer Academic, Dordrecht, 1996.

[4] Drew A. D. and Passman S. L. *Theory of multicomponent fluids.* Springer, NY, 1999.

[5] Drew D. A. Mathematical modeling of two-phase flow, *Ann Rev. Fluid Mech.*, 15 (1983), 261-291.

[6] E, W., Ren, W, and Vanden-Eijnden, A general strategy for designing seamless multiscael methods. *J. Comp. Phys.*, 228 (2009), 5437-5453.

[7] Fridman V. A method of successive approximations for Fredholm integral equations of the first kind (Russian). Uspekhi Mat. Nauk, 11 (1956), 233-234.

[8] Friesecke G. and Theil F. Validity and failure of the Cauchy-Born hypothesis in a two-dimensional mass-spring lattice, *J. Nonlinear Sci.*, 12, No. 5, (2002), 445-478.

[9] Groetsch C. W. *The Theory of Tikhonov Regularization for Fredholm Equation of the First Kind.* Pittman, Boston, 1984.

[10] Hardy, R.J. Formulas for determining local properties in molecular-dynamics simulations: shock waves. *J. Chem. Phys.*, 76 (1982), 622-628.

[11] Hansen, P. C. *Rank-Deficient and Discrete Ill-Posed Problems: Numerical Aspects of Linear Inversion.* SIAM, 1987.

[12] Irving J.H., and Kirkwood, J.G. The statistical theory of transport processes IV. The equations of hydrodynamics. J. Chem. Phys. 18 (1950), 817-829.

[13] Jikov V. V., Kozlov V. M., and Oleinik O.A. *Homogenization of Differential Operators and Integral Functionals.* Springer Verlag, New York, 1994.

[14] Joseph D. D. *Interrogations of direct simulation of solid-liquid flows.* E-book, available at `http://www.efluids.com/efluids/books/efluids-books.htm`, (2002), updated 2005.

[15] Kevrekidis I. G., Gear C.W., Hyman J.M., Kevrekidis P.G., Runborg O., and Theodoropoulos C. Equation-free, coarse-grained multiscale computation: enabling microscopic simulators to perform system-level analysis, *Commun. Math. Sci.*, 1 (2003) 715.

[16] Kirsch A. *An Introduction to the Mathematical Theory of Inverse Problems.* Springer, New York, 1996.

[17] Landweber L. An iteration formula for Fredholm integral equations of the first kind. Am. J. Math., 73 (1951), 615-624.

[18] Lavrent'ev, M. M., Romanov, V. G., and Shishatskij, S. P. *Ill-posed problems of mathematical physics and analysis.* American Mathematical Society, Providence, RI, 1980.

[19] Lehoucq, R. B, and Sears, M. P. The statistical mechanical foundations of the peridynamic nonlocal continuum theory: energy and momentum conservation laws. *Phys. Rev. E*, to appear.

[20] Love A. E. H. *A treatise on the mathematical theory of elasticity.* Dover, New York, 1977.

[21] Miller R. E. and Tadmor E. B. The quasicontinuum method: Overview, applications and current directions. *Journal of Computer-Aided Materials Design*, 9 (2002), 203239.

[22] Monaghan, J. Smoothed particle hydrodynamics, *Rep. Progr. Phys.* 68 (2005) 1703 – 1759.

[23] Morozov V. A. *Methods for Solving Incorrectly Posed Problems.* Springer, New York, 1984)

[24] Morris J., Fox P., Zhu Y., Modeling low Reynolds number incompressible flows using sph, *J. Comput. Phys.* 136 (1997), 214.

[25] Murdoch, A. I. and Bedeaux, D. Continuum equations of balance via weighted averages of microscopic quantities, *Proc. Royal Soc. London A*, **445**, (1994), 157-179.

[26] Murdoch, A. I. and Bedeaux, D. A microscopic perpsective on the physical foundations of continuum mechanics–Part I: macroscopic states, reproducibility, and macroscopic statistics, at presctribed scales of length and time. *Int. J. Engng Sci.* 34, No. 10 (1996), 1111-1129.

[27] Murdoch, A. I. and Bedeaux, D. A microscopic perpsective on the physical foundations of continuum mechanics II: a projection operator approach to the separation of reversible and irreversible contributions to macroscopic behaviour. *Int. J. Engng Sci.* 35, No. 10/11 (1997), 921-949.

[28] Murdoch, A. I. A Critique of Atomistic Definitions of the Stress Tensor, *J. Elasticity*, **88**, (2007), 113–140.

[29] Noll W. Der Herleitung der Grundgleichungen der Thermomechanik der Kontinua aus der statistischen Mechanik, *J. Rat. Mech. Anal.*, 4, (1955), 627-646.

[30] Panchenko A., Barannyk L. L., and Cooper K. Deconvolution closure for mesoscopic continuum models of particle systems, submitted to *Multiscale Model. Simul.*, preprint at arXiv:1109.5984.

[31] Panchenko A., Barannyk L. L., and Gilbert R. P. Closure method for spatially averaged dynamics of particle chains. *Non-linear Analysis: Real World Applications*, 12 (2011), 1681-1697.

[32] Seleson P., Parks M. L., Gunzburger M., and Lehoucq R. B., Peridynamics as an upscaling of molecular dynamics. *Multiscale Modeling and Simulation*, 8 (2009), No. 1, 204-227.

[33] Silling, S., and Lehoucq R. B. Peridynamic theory of solid mechanics. *Advances in Applied Mechanics*, 44 (2010), 73-168.

[34] Tadmor, E. B. , Ortiz M. and Phillips R. Quasicontinuum analysis of defects in solids *Philosophical Magazine A*, 73 (1996), 15291563.

[35] Tartakovsky A. M., Ferris K. F., Meakin P. Multi-scale lagrangian particle model for multiphase flows, *Computer Physics Communications*, 180 (2009), 1874–1881.
[36] Tartakovsky A, Panchenko A. and Ferris K. Dimension reduction method for ODE fluid models *J. Comp. Phys.*, 230, (2011), 8554-8572.
[37] Tartakovsky A. M., Meakin P. Pore-scale modeling of immiscible and miscible flows using smoothed particle hydrodynamics, *Advances in Water Resources*, 29 (2006,) 1464-1478.
[38] Tikhonov A. N. and Arsenin V. Y. *Solutions of Ill-Posed Problems*. Wiley, New York, 1987.
[39] Whitaker S. *The Method of Volume Averaging*, Kluwer Academic Press, Dordrecht, 1999.